Available online at www.sciencedirect.com

ScienceDirect

Geochimica et Cosmochimica Acta 286 (2020) 404–417

Geochimica et Cosmochimica Acta

www.elsevier.com/locate/gca

Discovery of coesite from the martian shergottite Northwest Africa 8657

Sen Hu [a,b,c,*], Yang Li [d], Lixin Gu [a], Xu Tang [a], Ting Zhang [a], Akira Yamaguchi [e], Yangting Lin [a,b,c], Hitesh Changela [a]

[a] Key Laboratory of Earth and Planetary Physics, Institute of Geology and Geophysics, Chinese Academy of Sciences, Beijing 100029, China
[b] Innovation Academy for Earth Science, Chinese Academy of Sciences, Beijing 100029, China
[c] College of Earth and Planetary Sciences, University of Chinese Academy of Sciences, Beijing 100049, China
[d] Center for Lunar and Planetary Sciences, Institute of Geochemistry, Chinese Academy of Sciences, Guiyang 550081, China
[e] National Institute of Polar Research, Tokyo 190-8518, Japan

Received 12 October 2019; accepted in revised form 11 July 2020; available online 22 July 2020

Abstract

We report occurrences of coesite in a martian meteorite, expanding previously-reported silica polymorphs such as stishovite (El Goresy et al., 2000), seifertite (Sharp et al., 1999; Goresy et al., 2008), and post-stishovite (El Goresy et al., 2000). The coesite was found in the shock-induced melt regions of NWA 8657, usually coexisting with deformed quartz and silica glass. Three morphological types of coesite have been identified: (I) in a silica-maskelynite assemblage, (II) needle grains, and (III) granular grains embedded in maskelynite. Transmission Electron Microscopy (TEM) shows that all types of coesite appear distributed in silica glass and/or nano-phase maskelynite. The stishovite-like morphology of Type II coesite and the presence of deformed quartz suggest coesite to have inverted from stishovite during decompression. The impact-induced peak pressures and temperatures are estimated at ~ 18–30 GPa and ~2000 ℃ respectively, based on static high pressure experiments (Langenhorst and Deutsch, 2012; Zhang et al., 1996). The polymorphs aggregates of silica in NWA 8657 indicate that the shock-induced melts in this meteorite cooled slower than those in other stishovite-bearing martian meteorites, but fast enough to preserve coesite.

Keywords: Mars; Shock metamorphism; Coesite; Plagioclase

1. INTRODUCTION

Coesite, a shock-induced high pressure polymorph of silica, occurs in lunar meteorties (Ohtani et al., 2011), HED meteorites (Miyahara et al., 2014), chondrites (Kimura et al., 2017; Weisberg and Kimura, 2010), and many terrestrial impact craters (Spray and Boonsue, 2009, 2018; Chao et al., 1960; El Goresy et al., 2001; Stähle et al., 2008; Chen et al., 2010; Fazio et al., 2017; Jaret et al., 2017). On the other hand, martian meteorites such as basaltic shergottites commonly experienced intensive shock-induced metamorphism as did HEDs (Miyahara et al., 2014; Pang et al., 2016, 2018), lunar meteorites (Barrat et al., 2005; Zhang et al., 2010; Ohtani et al., 2011; Miyahara et al., 2013a; Kayama et al., 2018), and chondrites (Stöffler et al., 1991, and references therein). More than 14 high pressure polymorphs have been reported in martian meteorites (Miyahara et al., 2011, 2016; Ma et al., 2015, 2016, 2018; Sharp et al., 2015, 2019; Langenhorst and Poirier, b, 2000a; Beck et al., 2004; Fritz and Greshake, 2009; Imae

* Corresponding author at: 19 Beituchengxi Road, Chaoyang District, Beijing 100029, China.
E-mail address: husen@mail.iggcas.ac.cn (S. Hu).

https://doi.org/10.1016/j.gca.2020.07.021
0016-7037/

and Ikeda, 2010; Aoudjehane et al., 2012; Baziotis et al., 2013; El Goresy et al., 2013; Greshake et al., 2013; Walton, 2013; Walton et al., 2014; He et al., 2015; Tomioka and Miyahara, 2017), including 3 high pressure polymorphs of silica, e.g., stishovite (El Goresy et al., 2000), seifertite (Sharp et al., 1999; Goresy et al., 2008), and baddeleyite structure SiO_2 (El Goresy et al., 2000). Formation of stishovite, seifertite, and baddeleyite structure SiO_2 requires much higher pressure than coesite. The absence or rareness of coesite is not attributable to a lower degree of shock metamorphism of martian meteorites than others, but to different post-shock thermal histories of the heavily shocked meteorites (Walton, 2013; Hu and Sharp, 2017). Coesite is theoretically able to form by three potential paths in silica and silicate phase diagrams (Zhang et al., 1996; Langenhorst and Deutsch, 2012; Ono et al., 2017): (1) back transformation from a higher pressure silica polymorph, *e.g.*, stishovite (Dachille et al., 1963; Zhang et al., 1996; Liu et al., 2018); (2) transformation of silica phases (e.g., tridymite, cristobalite, and quartz) to coesite by relative lower-speed impact, as reported in some terrestrial impact craters (Chao et al., 1960; Chen et al., 2010; Jaret et al., 2017); or (3) dissociation of plagioclase under high pressure conditions (Ozawa et al., 2014; Tomioka and Miyahara, 2017; Zhou et al., 2017) and zircon (Kaiser et al., 2008). In this work, we found various morphologies of coesite in martian meteorites, and conducted detailed petrographic, Raman, and TEM observations on the silica phases. The formation mechanisms of coesite and its preservation are discussed, which shed light on the unique post-impact thermal history of the more heavily shocked martian meteorites.

2. SAMPLE AND METHODS

2.1. Sample

A $\sim$ 10 g fragment of Northwest Africa (NWA) 8657 was bought from a Moroccan dealer in 2015. The sample used in this work is a polished thick section of the martian meteorite NWA 8657, with a total surface area of $\sim$3 cm^2 (Fig. S1). NWA 8657 was found in 2014, probably paired with NWA 8656 (Irving et al., 2015). NWA 8657 was later characterized as an enriched basaltic shergottite with large shock-induced melting regions (Hu et al., 2016; Howarth et al., 2018).

2.2. Analytical methods

2.2.1. SEM and EPMA

Scanning electron microscopy (SEM) imaging and energy dispersive X-ray spectroscopy (EDS) mapping were conducted using a field emission SEM *Nova NanoSEM 450* at the Institute of Geology and Geophysics, Chinese Academy of Sciences (IGGCAS), a *SUPRA55* at the National Astronomical Observatories, Chinese Academy of Sciences (NAOC), and a JEOL JSM-7100F at the National Institute of Polar Research (NIPR), Japan. Quantitative analyses of maskelynite, melt inclusion glasses, silica glasses, coesite aggregates, and mesostasis were conducted by electron probe microanalysis (EPMA) with the JEOL JXA-8100 at IGGCAS. The accelerating voltage was 15 kV, and the beam current was 10 nA. The EPMA standards were natural and synthetic minerals: natural kaersutite for Si, Mg and Fe, jadeite for Na and Al, bustamite for Ca and Mn, and K-feldspar for K, synthetic rutile for Ti and Cr_2O_3 for Cr. X-ray interference of the K_α line of Mn by the K_β line of Cr was corrected. The Bence-Albee method was used for quantitative analysis. The detection limits are: 0.01 wt% for K_2O, 0.02 wt% for SiO_2, Al_2O_3, MgO, CaO, and Na_2O, 0.03 wt% for TiO_2 and Cr_2O_3, 0.05 wt% for FeO, and 0.06 wt% for MnO.

2.2.2. Raman

Raman spectra were obtained using a Renishaw RM-2000 type laser Raman spectrometer at the Technical Institute of Physics and Chemistry, Chinese Academy of Sciences. A 532 nm wavelength Ar ion laser was used, with the beam focused on $\sim$1 μm spot of the sample surface. The laser Raman spectrometer was calibrated with a single crystal silicon standard peak at 520.5 cm^{-1}. The laser power was 5 mW (10 % percent of the maximum) to prevent vitrification during analyses. In this study, Raman has been useful for the identification of different silica polymorphs.

2.2.3. FIB

Ultrathin foils (about $10 \times 3 \times 0.1$ μm^3 and $10 \times 5 \times 0.1$ μm^3) of selected regions were prepared by focused ion beam-scanning electron microscope (FIB-SEM). Focused ion beam TEM sample prepration was conducted on a Zeiss *Auriga Compact* dual beam at IGGCAS and the FEI Scios Dual beam system at the Institute of Geochemistry, Chinese Academy of Sciences (GYIGCAS) using traditional FIB preparation techniques. A layer of Pt was deposited over the region of interest to protect the surface from ion beam damage during sample preparation. After cutting, the TEM foil was lifted out using an Omniprobe 200 micromanipulator and attached to a copper grid. Ion milling was carried out with an accelerating voltage of 30 kV and beam currents of 7 nA. Final polishing of the thin foil was conducted at 5 kV with a beam current of 50 pA.

2.2.4. TEM

Transmission Electron Microscopy analyses were performed with an FEI *Talos* F200X and Tecnai F20 with accelerating voltages at 200 kV, at the Suzhou Institute of Nano-tech and Nano-bionics, Chinese Academy of Sciences. The microstructure of the FIB foils was analyzed by both dark field (DF) TEM and the high-angle annual dark field scanning transmission electron microscopy (HAADF-STEM). Elemental and chemical analyses of the foils were performed by TEM-EDS on the Talos F200X, named super-X, with four windowless X-ray detectors. DF-TEM imaging, selected area electron diffraction (SAED) and high-resolution transmission electron microscopy (HRTEM) imaging were carried out using a JEOL JEM-2100 operated at 200 kV, electron beam generated from a LaB_6 gun at the IGGCAS. The phases in the FIB foils were identified by combining EDS mapping,

high-resolution TEM images with fast Fourier transformation (FFT), and selected area electron diffraction (SAED).

3. RESULTS

3.1. Petrography of NWA 8657

The NWA 8657 thick section has a texture characteristic of a basaltic shergottite, mostly composed of pigeonite, augite, and maskelynite, with minor phosphates, ilmenite, titanomagnetite, mesostasis, and trace silica (Fig. S1). In this paper, the term "maskelynite" refers to any amorphous material of feldspathic composition (Table S1) either as quenched melt or diaplectic glass. Pyroxene shows a patchy texture as the intergrowth of pigeonite and augite without a clear boundary. The petrographic texture of NWA 8657 is similar to that previously reported (Howarth et al., 2018). However, 4 large shock melt zones (up to ~6 mm^2) (yellow circles in Fig. S1) across ~5 % of the section were identified.

Silica phases in NWA 8657 mainly occur in mesostasis (Fig. 1d), interstitial areas between maskelynite and pyroxene (Fig. S2), and melt inclusions enclosed by ilmenite and titanomagnetite (Fig. 2a and b). Such textures are consistent with those reported in other basaltic shergottites (El Goresy et al., 2013; Jambon et al., 2002; Leroux and Cordier, 2006). Almost all silica phases have been transformed to glass (Fig. 3i and S2) except a few high-pressure polymorphs and quartz (Fig. 3a–h, 4a, 4c–e, and 4g–j) found in large melt zones and pockets.

3.2. The occurrences of coesite

Three types of occurrences of coesite were found in two large shock melt zones (Fig. S1).

Type I coesite was found in a silica (dark grey) and maskelynite (light grey) assemblage (Fig. 1a and b), close to the boundary of the melt zone and the host rock (Fig. S1). This assemblage is surrounded by fine grained pyroxene recrystallized from shock induced melt (Fig. 1b). Silica grains in the assemblage show subhedral textures with grain sizes in micrometers (Fig. 1b). In contrast, maskelynite (feldspathic domains) is mainly filling in the interstitial areas of silica grains (Fig. 1b), agglutinating micron-sized silica grains to form the assemblage. Nanometer-sized vesicles were observed only in maskelynite in the central region of the assemblage (white arrow in Fig. 1b).

Three Raman analyses (R34, R90 and R91 in Fig. 1b) are measured on this assemblage from the central region towards the rims. Raman spectra show strong peaks at ~521 cm^{-1} and other weak peaks at 467, 426, 356, 310, 266, 203, 173, 150, and 117 cm^{-1} (Fig. 3a–c), suggesting the major crystalline phase in this assemblage is coesite (Sharma et al., 1981). A minor Raman peak at 461 cm^{-1} was observed in the central area of the assemblage (Fig. 3a).

Type II coesite was found in two separate locations; in the fine grained matrix around Type I coesite (Fig. 1a and b), and within another melt pocket (Fig. 1c–f). Type II coesite displays micron-submicron needle-like morphologies as well as abundant euhedral micrometer-sized grains (likely the cross sections of needle grains) (Fig. 1). Hereafter we call this type of coesite as needle grains. These needle grains are usually set in the matrix of the melted areas which are mainly composed of fine grained pyroxene and some relict pyroxene and maskelynite grains (Fig. 1). The morphology of Type II coesite is similar to stishovite reported in NWA 480, NWA 856, and other martian meteorites (Chennaoui Aoudjehane et al., 2005; El Goresy et al., 2001).

Two Raman spectra measured (Fig. 3g and h) on these needle grains (R58 and R62 in Fig. 1d) show two strong peaks at 667 and 998 cm^{-1} from the surrounding recrystallized pyroxene, as well as weak diagnostic peaks of coesite at 521 cm^{-1}. In addition, quartz is observed around the boundary of the melt pocket (Fig. 1e), with a Raman peak at 461 cm^{-1} (Fig. 3d–f). Silica phase in the adjacent mesostasis (Fig. 1d) has broad Raman peaks characteristic of silica glass at 455, 491, 602, and 810 cm^{-1} (Fig. 3i).

Type III coesite, up to ~10 μm in length and ~6 μm in width in BSE images, has a granular texture embedded in maskelynite (Fig. 2). It was found in two separate locations in the largest melt zone (Fig. S1): (1) in a melt inclusion enclosed by titanomagnetite (Fig. 2a and b) in the central area of the melt zone (Fig. S1) and (2) adjacent to the boundary of the melt zone (Fig. S1). These coesite grains have zonation in BSE images with brighter contrast along the margins and darker contrast inside them (Fig. 2). Coesite occurring in the melt inclusion has Raman peaks at 520, 467, 426, 356, 329, 266, 203, 173, and 150 cm^{-1} (Fig. 4c–e), almost identical to that of Type I coesite. The co-occurring maskelynite and outer parts associated with titanomagnetite show broad Raman bands at ~500 and ~680 cm^{-1} (Fig. 4a and b). The Raman spectrum of maskelynite also displays a peak at 520 cm^{-1} (Fig. 4a), attributable to the inclusion of adjacent coesite during analysis. An additional shock melt zone has coesite similar in texture to those found in the melt inclusion, displaying granular shapes (Fig. 2) and Raman peaks at 1033, 520, 467, 426, 356, 266, 173, and 150 cm^{-1} (Fig. 4g, i, and j). Quartz was only identified in this location, with a Raman peak at 459 cm^{-1} and several small peaks at 522, 394, 186, and 121 cm^{-1} (Fig. 4g). Silica glasses are also confirmed by Raman with broad bands at ~500 cm^{-1} and weak broad peaks at 600 and 810 cm^{-1}, as well as some other weak peaks attributed to quartz and coesite at 459 cm^{-1} and 520 and 1033 cm^{-1}, respectively (Fig. 4h and i). The surrounding merrillite and pyroxene grains have sharp Raman peaks at 971 and 956 cm^{-1} (Fig. S3) and at 657 and 996 cm^{-1} respectively (Fig. 4k).

3.3. Results of TEM analysis of coesite

Three FIB foils were prepared from locations shown in Figs. 1b, 2b, and d. The FIB01 foil was cut from Type I coesite (Fig. 1b). It is mostly composed of subhedral silica glasses, maskelynite, and euhedral nanometer-sized pyroxene grains (Fig. 5a). Nanophase pyroxene grains (white arrow in Fig. 5a) are observed to coexist with maskelynite along the margins of the assemblage. Many spherical vesicles were found in maskelynite in the center of the

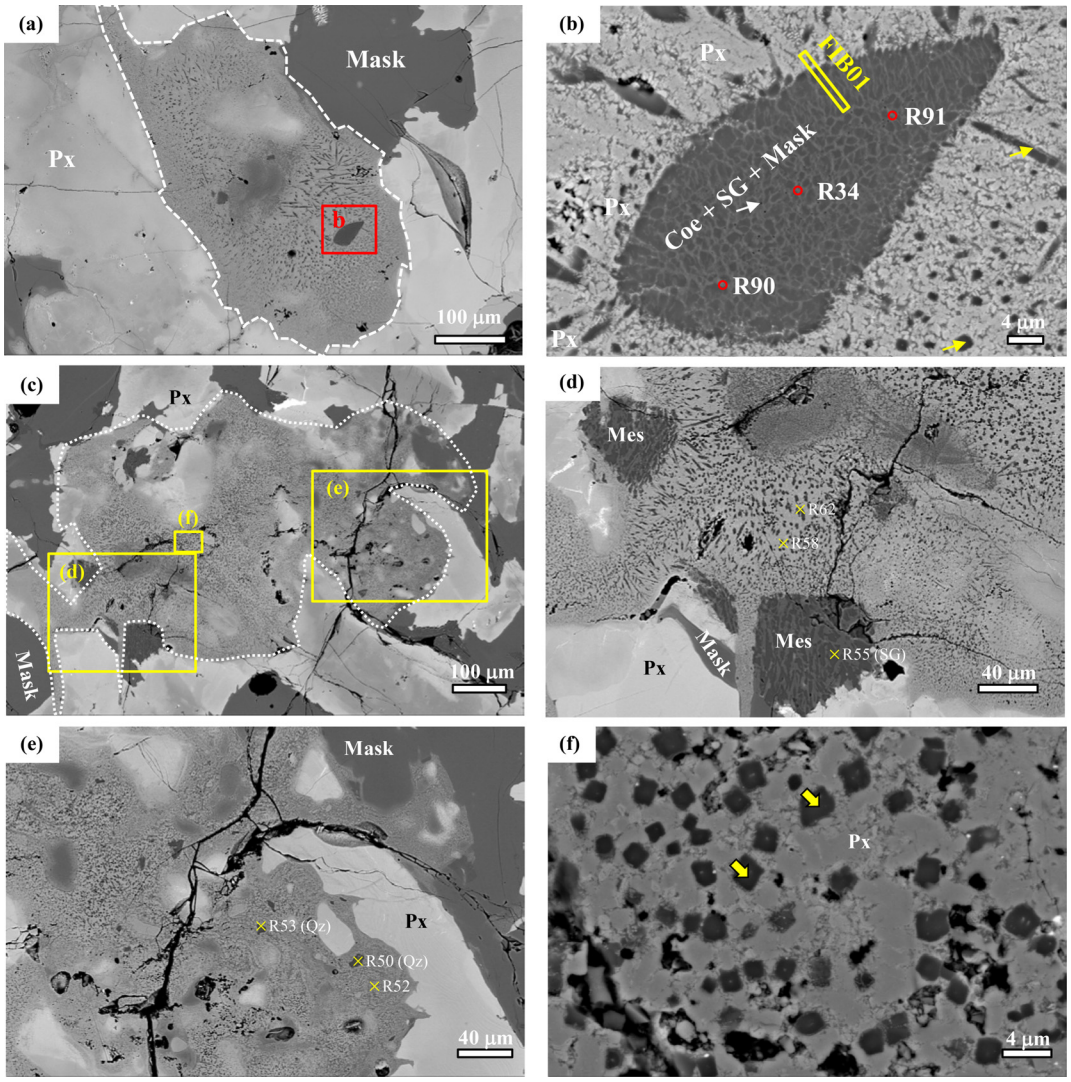

Fig. 1. Petrographic textures of Type I and Type II coesite. (a) The melt pocket (white dash line circled area) is mainly composed of micrometer-sized pyroxene, silica phases, felspathic glasses, and a silica-maskelynite assemblage (Type I coesite). (b) Higher magnification image of the assemblage of coesite, silica glass, and maskelynite. Silica glass is darker than maskelynite displaying a patchy texture around silica glass. Spherical vesicles (white arrow in Fig. 1b) occur only in the central parts of the assemblage and are absent inside silica glass. Type II coesite, needle shaped silica phases (or euhedral silica grains by cross cut in BSE, yellow arrows in Fig. 1b), occurs in the adjacent matrix which is mostly recrystallized pyroxene. The locations of the FIB foil and Raman analyses are marked. (c) Type II coesite found in another melt pocket, mostly recrystallized pyroxene, with silica and maskelynite. (d) Magnified BSE image outlined in (c). Needle shaped silica grains are concentrated along the boundary of the melt pocket. Euhedral silica grains are however ubiquitously distributed across the melt pocket and coarser in the central areas than along the rims. The adjacent mesostasis displays intergrowths of silica and maskelynite. Locations of Raman analyses of the silica phases are marked. (e) Location of deformed quartz in the inner border of the melt pocket outlined in (c). (f) Magnified BSE image of euhedral micrometer sized silica grains outlined in (c). Px: pyroxene, Mask: maskelynite, Coe: coesite, SG: silica glass, Mes: mesostasis, Qz: quartz. (For interpretation of the references to colour in this figure legend, the reader is referred to the web version of this article.)

assemblage that are not found in the inner area of the smooth silica glasses and surrounding melt zones (Fig. 5). The nanometer-sized coesite (~10–60 nm) occurs in the maskelynite area and is absent in smooth silica glasses (Fig. 5h). Selected Area Electron Diffraction (SAED) patterns are consistent with a fine-grained aggregate of maskelynite and coesite.

The FIB02 foil prepared from Type III coesite in the melt inclusion (Fig. 2b) mostly contains silica phases, maskelynite, titanomagnetite, and clinopyroxene (Fig. 6a). The granular grain of Type III coesite indicated by Raman is an aggregate of silica glass and nanometer-sized coesite (~10–70 nm) shown as the brighest areas in the dark field TEM image (Fig. 6b). The coesite-bearing silica aggregates are enclosed by maskelynite. The SAED pattern of the biggest coesite grain is shown in Fig. 6c. The FIB03 foil was cut from the area shown in Fig. 2d and has a similar texture to FIB02, with nanometer-sized coesite (~10–50 nm)

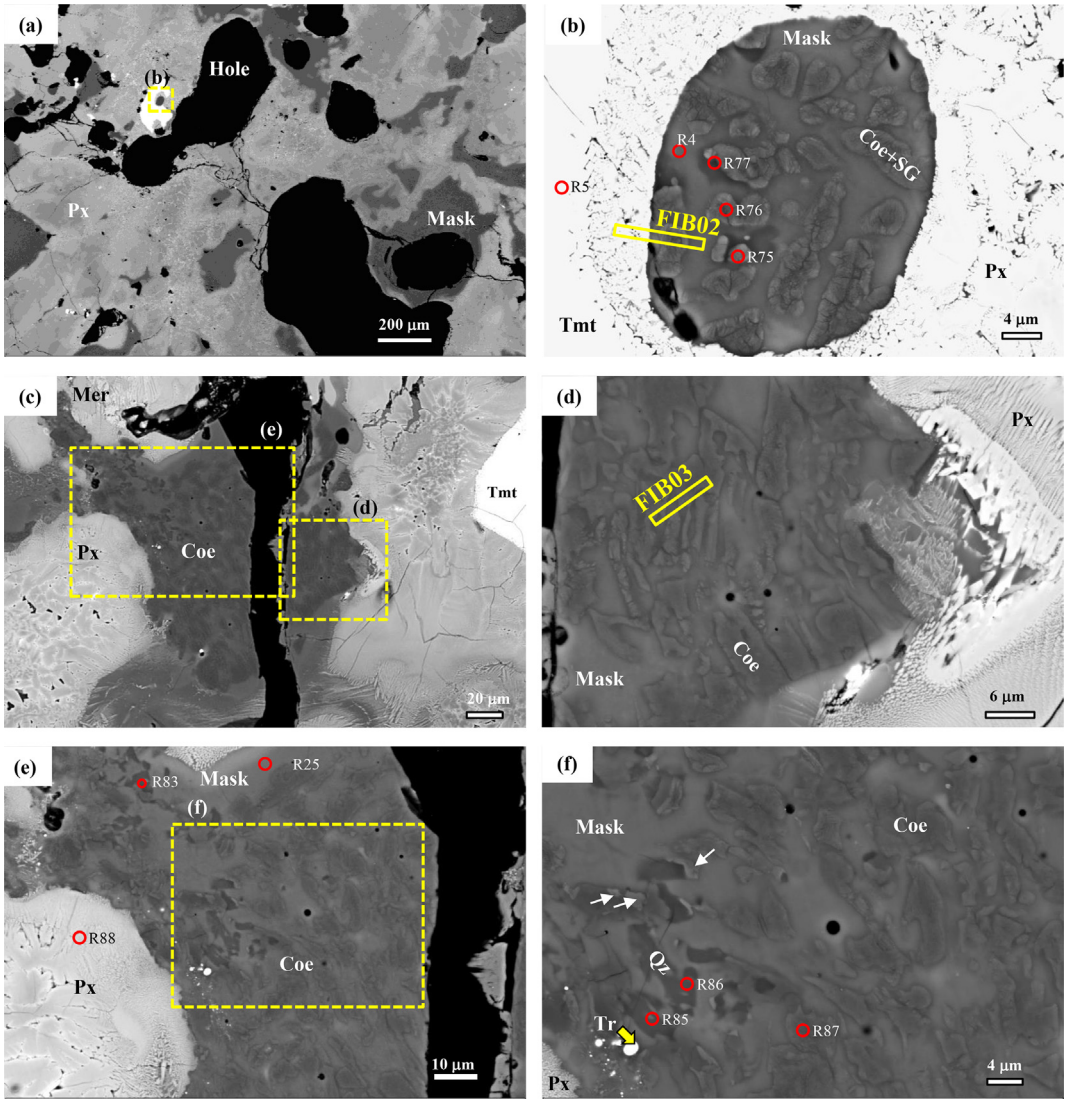

Fig. 2. Petrographic textures of Type III coesite found in two locations. (a) Coesite occurs in a melt inclusion enclosed by a titanomagnetite. The matrix displays a flow texture of maskelynite and clearly shows pyroxene recrystallization. Some voids are also noticeable. (b) Magnified BSE image of the melt inclusion. Coesite, enclosed within the maskelynite, has granular textures (up to several micrometers in width and 10 micrometers in length), displaying zonation, with higher contrast along the rims and lower contrast in the central areas. The locations of Raman analyses and FIB foil extractions are marked on this image. (c) Coesite as the major phase in maskelynite. (d) Magnified image of coesite from (c). Coesite has similar textures to that found in the melt inclusion. Spherical vesicles are observed in maskelynite. (e) Magnified BSE image of the region shown in (c). Two types of silica phases occur. (f) Magnified image of local area in (e). Spherical vesicles and troilite (yellow arrow) occurring in maskelynite. Quartz (darker in BSE) displays subhedral textures, coexisting with coesite (White arrows). Px: pyroxene, Mask: maskelynite, Coe: coesite, SG: silica glass, Tmt: titanomagnetite, Tr: troilite, Qz: quartz. (For interpretation of the references to colour in this figure legend, the reader is referred to the web version of this article.)

co-occurring with silica glass (Fig. S4). Tiny coesite grains show different orientations as well (Fig. S4).

3.4. Shocked features of plagioclase

Crystalline plagioclase is relatively rare in shergottites (e.g., NWA 8159; Herd et al., 2017). We identified a few grains of plagioclase with sizes up to 5 μm and subhedral shapes in NWA 8657. The plagioclase shown in Fig. 7a and b co-occurs with maskelynite embedded in fine grained matrix displaying widespread recrystallization of pyroxene. This plagioclase is darker than the contacting maskelynite by BSE (Fig. 7b). Some bright phases comparable to matrix pyroxene are observed along the grain boundary and inside the grain (Fig. 7b). The occurrences of the plagioclase in NWA 8657 are similar to that of the second textural type tissintite found in Tissint (Ma et al., 2015). However, plagioclase in NWA 8657 is darker than co-occurring maskelynite (Fig. 7a and b) by BSE, opposite to the occurrences of tissintite and maskelynite in Tissint (Ma et al., 2015). Moreover, plagioclase in NWA 8657 has a strong Raman peak at 500 cm^{-1}, with minor peaks at 163, 224, 670, and 1014 cm^{-1} (Fig. 7c), significantly different to that of tissintite (Ma et al., 2015). The surrounding fine grained matrix is

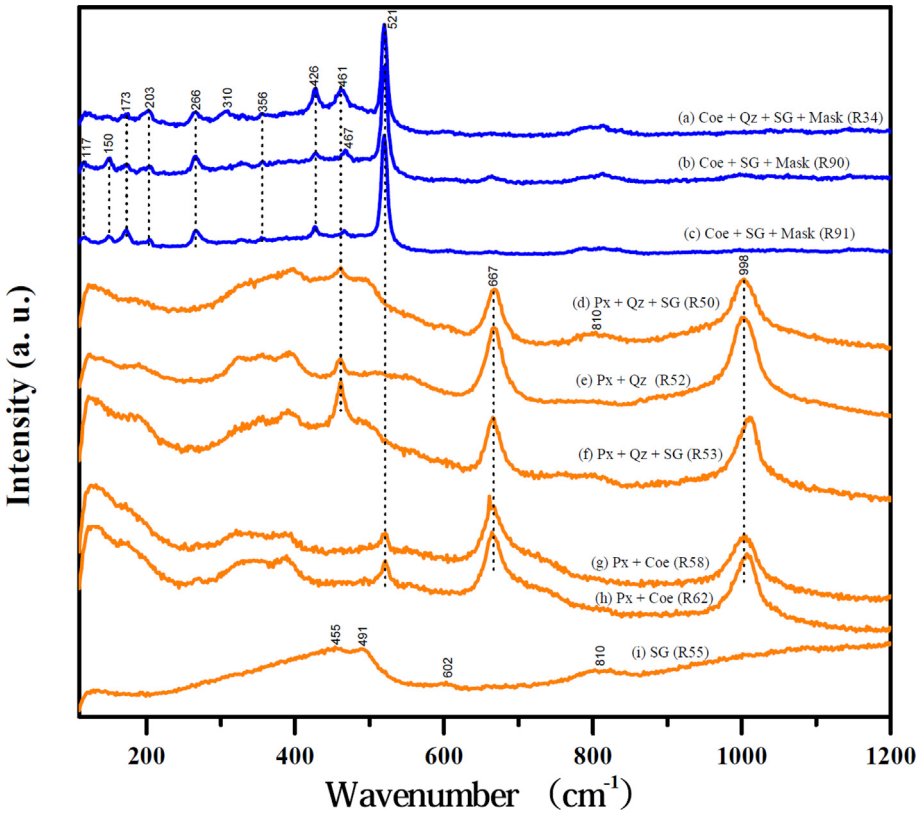

Fig. 3. Raman spectra of various phases from Type I (a-c) and Type II coesite (d-i). (a)-(c) Raman spectra of the coesite measured from the silica-maskelynite assemblage. Raman sharp peaks at 521, 461, 426, 356, 310, 266, 203, 173, 150, and 125 cm^{-1} are indicative of coesite. (d)-(f) Raman spectra of quartz with pyroxene measured from the locations shown in Fig. 1e. Quartz shows the diagnostic Raman peak at 461 cm^{-1}. (g) and (h) Raman spectra of euhedral coesite grains with pyroxene. The Raman spectra display peaks at 521, 667, and 998 cm^{-1}. (i) Raman spectra of silica glass in the adjacent mesostasis outlined from the locations shown in Fig. 1d. Coe: coesite, Qz: quartz, Mask: maskelynite, SG: silica glass, Px: pyroxene.

mainly composed of pyroxene and maskelynite (Fig. 7c, R41). A merrillite grain in the melt pocket displays strong Raman peaks at 958 and 973 cm^{-1} with minor peaks at 410, 449, 667, 755, 1013, and 1082 cm^{-1} (Fig. 7c, R17). The patchy pyroxene from the host rock has strong Raman peaks at 665 and 1007 cm^{-1} with minor peaks at 318 and 393 cm^{-1} (Fig. 7c, R17).

FIB04 was prepared from plagioclase in the area shown in Fig. 7b. HAADF imaging shows the plagioclase to have a smooth surface, and to be darker than the other silicates and mafic glasses, attributable to its lower Mg and Fe concentrations (Fig. 8). The fine grained matrix is mainly composed of nanometer-sized (<200 nm) euhedral pyroxene grains and maskelynite (Fig. 8a). Some pyroxene grains occur in the inner areas of plagioclase (Fig. 8a). The glasses located in the lower central region have higher Fe, lower Ca and identical Si and Mg content compared with the plagioclase (Fig. 8b–e). Two interfaces of the plagioclase are significantly enriched in Fe (Fig. 8b). SAED patterns on different plagioclase gains (Fig. 8a) indicate that they may be a single crystal with the same orientation.

3.5. Mineral chemistry

The chemical compositions of coesite, silica glass, plagioclase, maskelynite, mesostasis, and melt inclusions from NWA 8657 are listed in Table S1. The coarse silica glass grains occurring in interstitial regions (Fig. S2) are mainly composed of SiO_2 (92.9 wt%) with minor Al_2O_3 (2.5 wt %), FeO (0.3 wt%), TiO_2 (0.24 wt%), CaO (0.5 wt%), Na_2O (0.7 wt%), and K_2O (0.2 wt%) (Table S1). The coesite-bearing aggregates have lower SiO_2 (87.9 wt%) and higher Al_2O_3 (4.6 wt%), FeO (1.43 wt%), CaO (1.0 wt%), Na_2O (1.1 wt%), and K_2O (0.7 wt%) content than the silica glass (Table S1). Melt inclusion glasses (MIs) and the mesostasis (Mes) have similar SiO_2 (~75 wt%) and K_2O (3.1–3.4 wt%) content, but vary more in Al_2O_3 (MI: ~10.2 wt%, Mes: ~15.1 wt%), FeO (MI: ~3.2 wt%, Mes: ~0.8 wt%), CaO (MI: ~0.6 wt%, Mes: ~2.3 wt%), and Na_2O (MI: ~2.4 wt%, Mes: ~3.3 wt%) (Table S1). Maskelynite and plagioclase have nearly identical chemical compositions mainly composed of SiO_2 (~55 wt%), Al_2O_3 (~26 wt%), CaO (~10 wt%), and Na_2O (~5 wt%) with minor K_2O and FeO (Table S1).

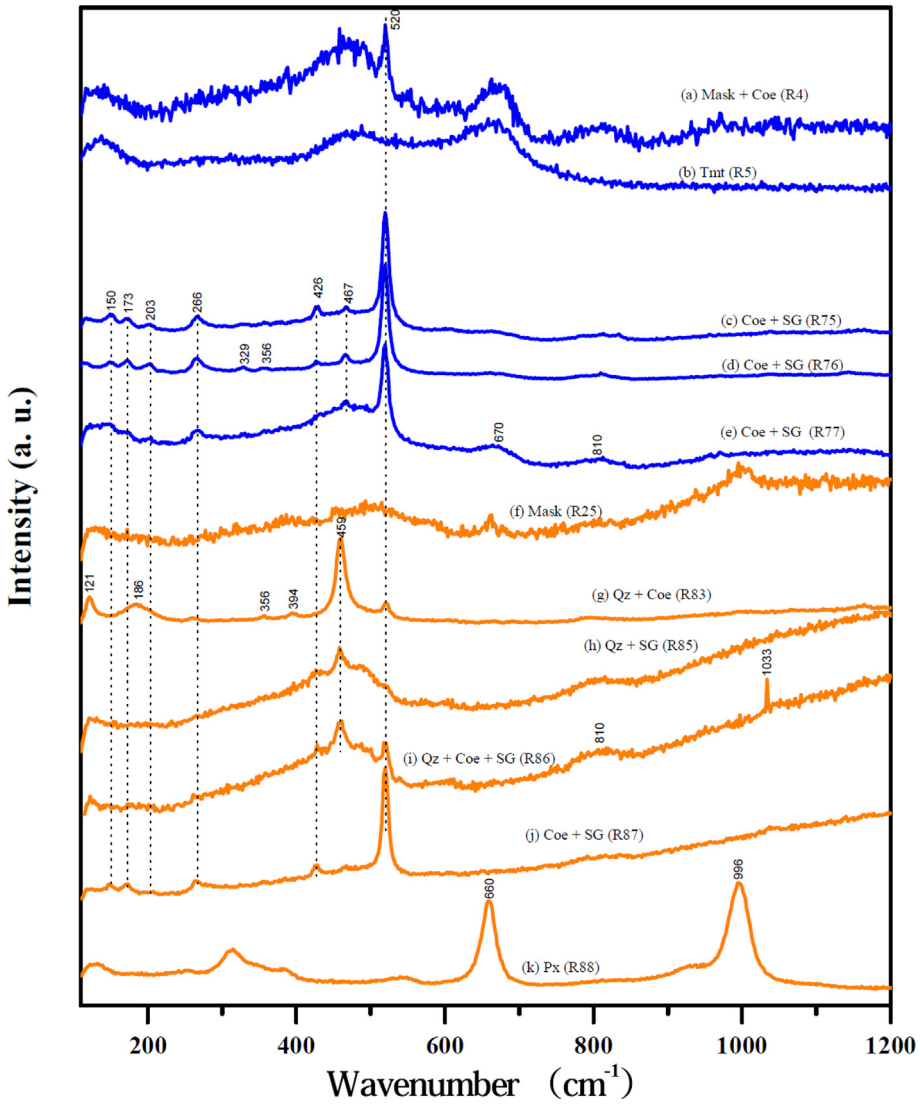

Fig. 4. Raman spectra of Type III coesite, (a) - (e) Coesite in the melt inclusion in Fig. 2b and (f)-(k) the other locations in Fig. 2e and f. (a) Raman spectra of maskelynite with coesite. (b) Titanomagnetite (Tmt). (c)–(e) Coesite with silica glass. (f) Maskelynite. (g) Quartz with coesite. (h) Quartz with silica glass. (i) Coesite with silica glass. (j) Coesite with silica glass. (k) Adjacent recrystallized pyroxene.

4. DISCUSSION

4.1. Coesite formation mechanisms

Coesite has several possible formation pathways based on the silica and silicate phase diagrams (Kaiser et al., 2008; Langenhorst and Deutsch, 2012; Ono et al., 2017; Tomioka and Miyahara, 2017; Zhang et al., 1996): (1) back transformation from a higher pressure silica polymorph, such as stishovite (Dachille et al., 1963; Zhang et al., 1996; Liu et al., 2018); (2) formation from silica phases by relatively lower-impact speeds, as found in some terrestrial impact craters (Chao et al., 1960; Chen et al., 2010; Jaret et al., 2017); or (3) decomposition products of plagioclase (Ozawa et al., 2014; Tomioka and Miyahara, 2017; Zhou et al., 2017) and zircon (Kaiser et al., 2008). The formation of coesite from either a silica melt (Kieffer et al., 1976; Stähle et al., 2008) *Vs.* solid-state transformation from diaplectic silica glass (Chao, 1967; Langenhorst, 1994; Stoffler and Langenhorst, 1994; Stähle et al., 2008) under high pressure (HP) and high temperature (HT) conditions is a matter of debate. Here we discuss the formation of the 3 distinctive types of coesite discovered in NWA 8657.

4.1.1. Type I Coesite (in a silica-maskelynite assemblage)

Silica glasses and K-rich maskelynite make up most of the Type I coesite assemblage (Fig. 1b and 5). This suggests that this assemblage was derived from the mesostasis. Type I coesite has diagnostic coesite Raman peaks (Fig. 3a–c). However, TEM shows that coesite co-occurs with maskelynite rather than being enclosed in silica glasses (Fig. 5). Maskelynite (probably quenched feldspathic glasses) in this assemblage displays patchy textures (Fig. 5a and b),

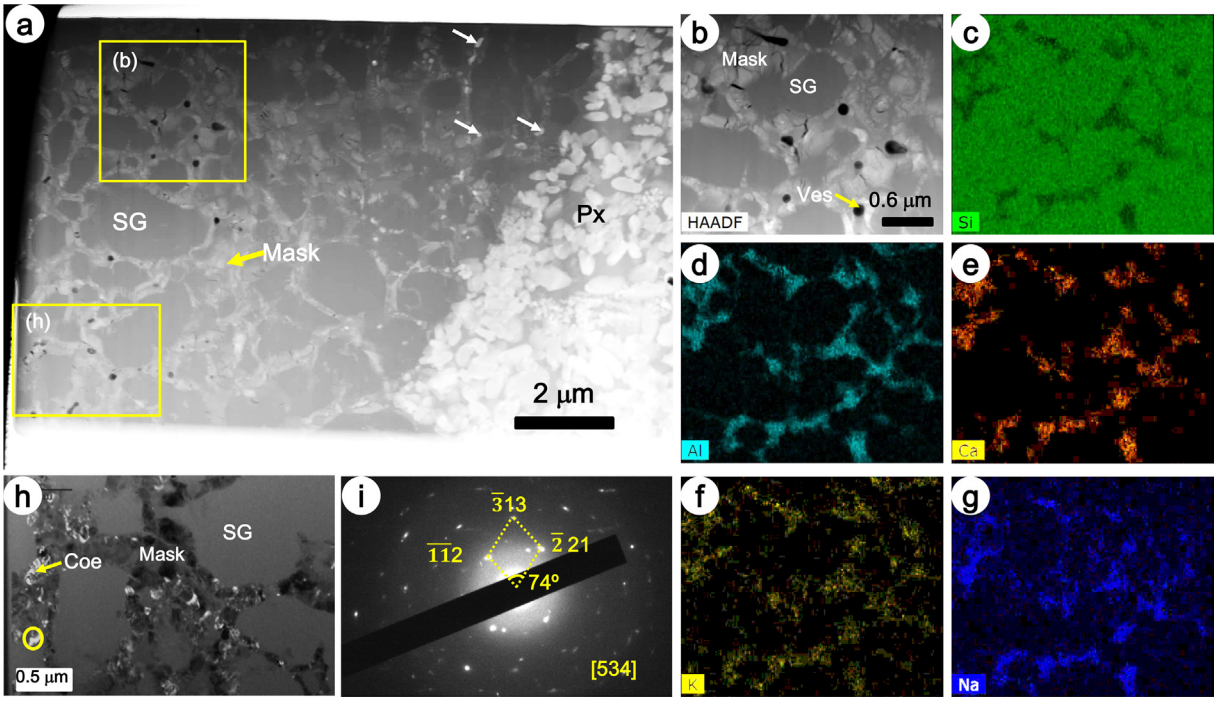

Fig. 5. TEM analysis of Type I coesite. (a) HAADF image of FIB01 foil from Type I coesite. Silica glass up to several microns in diameter has subhedral textures and occurs with maskelynite interstitial to silica glass. Vesicles occur in maskelynite and are absent in the coarse silica glass grains. Nanophase of pyroxene grains (white arrow) are observed to coexist with maskelynite along the margins of the assemblage. The surrounding matrix is mainly comprised of micron-sized pyroxene crystals. (b)-(g) HAADF image and EDS mapping of Si, Al, Ca, K, and Na respectively. Silica grains are lath-shaped at their margins and inter-penetrate with maskelynite. (h) Dark field TEM image of area outlined in (a). Coesite is nanophase (~10–70 nm) and co-occurs with maskelynite, but is absent in the inner areas of coarse silica glass. (i) SAED pattern of coesite circled in (h). The incident electron beam direction is marked at lower right. Px: pyroxene, Mask: maskelynite, SG: silica glass, Ves: vesicles, Coe: coesite.

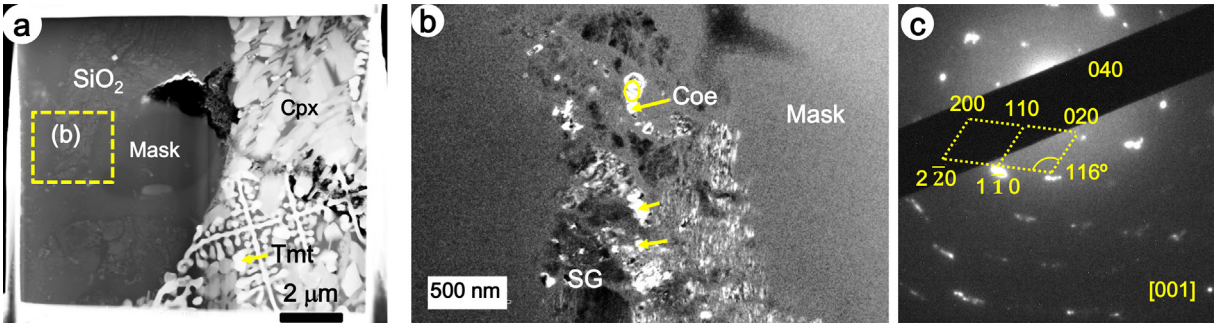

Fig. 6. TEM analysis of Type III coesite from the melt inclusion. (a) HAADF image of the FIB03 foil. Silica phases are enclosed by maskelynite. The rim is mainly comprised of micron-sized pyroxene and titanomagnetite. (b) Dark field TEM of coesite. Nanophase coesite (~10–60 nm) are brightest and co-occur with silica glass enclosed by maskelynite with smooth textures. (c) SAED pattern of coesite grains circled in (b). The incident electron beam direction is marked at lower right. Mask: maskelynite, Cpx: clinopyroxene, Tmt: titanomagnetite, Coe: coesite.

significantly different to that of typical maskelynite (e.g., Fig. 6b). This suggests that it was molten prior to quenching into glass - an observation also supported by tiny recrystallized pyroxene embedded the maskelynite (Fig. 5b). Incipient melting is suggested by the intergrowth of regular and 'furry' lath of maskelynite (Fig. 5b), which are absent in the typical mesostasis (Fig. 1d).

In shock-induced metamorphism, plagioclase has been found to dissociate to jadeite + silica (stishovite or coesite or amorphous silica) + Ca-Hexaluminosilicate phase (CAS) in some chondrites (Kimura et al., 2000; Miyahara et al., 2013b; Ozawa et al., 2014; Ohtani et al., 2017) and achondrites (El Goresy et al., 2004). However, in most cases, jadeite is more abundant than coesite and/or

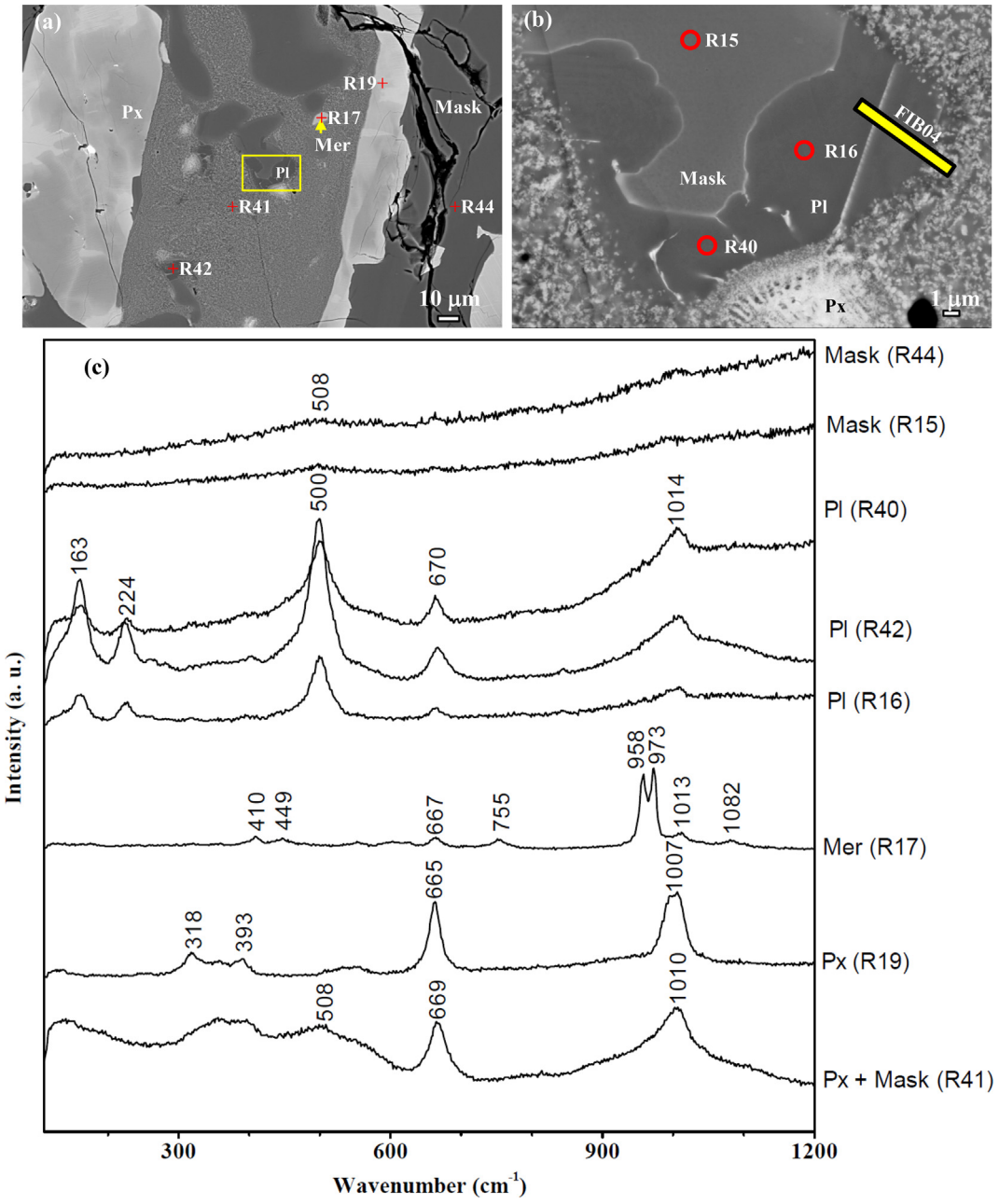

Fig. 7. Texture of plagioclase and associated Raman spectra. (a) A melt pocket containing plagioclase is mainly composed of fine-grained pyroxene and maskelynite, with several large pyroxene, maskelynite and merrillite clasts. (b) Magnified area of yellow rectangle outlined in (a). Plagioclase shows darker contrast than maskelynite enclosed by fine grained matrix. (c) Raman spectra of plagioclase, maskelynite, matrix, merrillite, and pyroxene marked in (a) and (b). Px: pyroxene, Mask: maskelynite, Pl: plagioclase, Mer: merrillite. (For interpretation of the references to colour in this figure legend, the reader is referred to the web version of this article.)

tishovite (Kimura et al., 2000; Miyahara et al., 2013b; Ozawa et al., 2014; Ohtani et al., 2017), and jadeite occurs usually without stishovite and/or coesite. The conditions for stishovite formation are unfavorable due to its sluggish nucleation rate compared with jadeite, leading to a heterogeneous and incomplete plagioclase dissociation reaction; plagioclase dissociates into jadeite + residual amorphous material (Miyahara et al., 2013b). Under longer HP and HT conditions (up to 4–5 s), coesite or stishovite should form, an example being the formations of coesite and jadeite in the NWA 8275 LL7 chondrite (Miyahara et al., 2017). Under much longer HP and HT conditions, stishovite will mostly form as shown by synthetic experimental predictions (Kubo et al., 2009). However, coesite, the only high pressure polymorph identified in NWA 8657, should crystallize from a silica melt rather than dissociation of

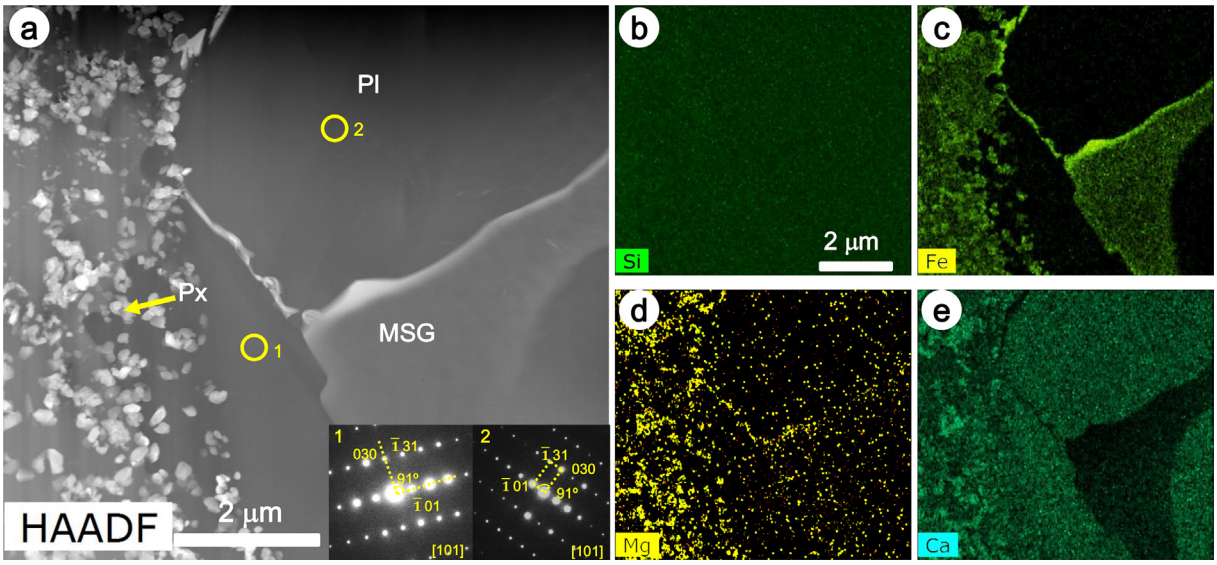

Fig. 8. TEM analysis of plagioclase. (a) HAADF image of FIB04 foil from locations shown in Fig. 7b. Inset images are SAED patterns acquired from the locations shown by yellow circles. The incident electron beam direction is marked at lower right. (b)–(e) are Si, Fe, Mg, and Ca distributions, respectively, corresponding to the area shown in (a). Px: pyroxene, Pl: plagioclase, MSG: mafic silicate glass.

plagioclase, otherwise, jadeite should have been identified by Raman and TEM (Kubo et al., 2008; Ohtani et al., 2017).

An alternative explanation for the formation of Type I coesite could be recrystallization from a feldspathic melt. However, in this case, the absence of jadeite with coesite is also difficult to explain (Kubo et al., 2008; Ohtani et al., 2017): Jadeite can form by either plagioclase dissociation (Miyahara et al., 2013b) or crystallization from plagioclase melt (Ozawa et al., 2014).

A plausible formation mechanism of Type I coesite is the crystallization of silica melt along the maskelynite-silica interface in mesostasis, which is consistent with the patchy textures of K-rich maskelynite (Fig. 5f and g) and incipient melting of large silica grains (Fig. 5a and b). Type I coesite may have crystallized from SiO_2-rich regions by incomplete mixing between silica and plagioclase melts in a short-lived shock event. This scenario is also consistent with the occurrence of coesite only in the outer melts rather than in inner areas of the smooth and coarse silica grains (Fig. 5h). These maskelynite and silica domains quenched into glasses upon post shock cooling.

4.1.2. Type II Coesite (needle grains)

The Type II coesite, needle shaped grains, around Type I coesite (Fig. 1a and b) as well as a melt pocket (Fig. 1c–f), has similar textures to stishovite observed in the basaltic shergottites NWA 480, NWA 856, and Shergotty interpreted to have crystallized from a melt (Chennaoui Aoudjehane et al., 2005; El Goresy et al., 2013). However, Raman peaks of stishovite on the needle shaped silica grains in NWA 8657 (Fig. 3g and h) are lacking. Rather, Raman peaks of coesite are found in the needle shaped silica grains (Fig. 3g and h). The needle shaped morphology of Type II coesite suggests it to have crystallized from a melt rather than solid-state transformation (Figs. 1 and 3) (Chennaoui Aoudjehane et al., 2005; El Goresy et al., 2013). This is also supported by synthetic experiments (Liu et al., 2007). The similar morphologies of Type II coesite in NWA 8657 with stishovite from the other martian meteorites (Chennaoui Aoudjehane et al., 2005; El Goresy et al., 2013) suggests that Type II coesite was likely formed from inversion of stishovite. This mechanism requires forming stishovite during a densification stage followed by stishovite inversion to coesite during decompression.

Silica phases such as quartz are scarce in martian meteorites (El Goresy et al., 2004; Leroux and Cordier, 2006). Cristobalite (or tridymite) could be the major original accessory silica phase crystallized from the parent magma of martian meteorites (El Goresy et al., 2004; Leroux and Cordier, 2006). In the case of NWA 8657, most silica domains have transformed to glasses by shock metamorphism (Fig. 3i and S2). Quartz observed around the melt pocket (Fig. 2e) with Raman peaks at 461 cm^{-1} (Fig. 4d–f), 3 wave numbers lower than the un-deformed quartz (at 464 cm^{-1}), suggests a formation by the complete back transformation of stishovite and/or partial coesite back transformation during compression (El Goresy et al., 2001). The absence of coesite Raman peaks on these quartz grains (Fig. 2d–f) suggests that the former scenario is more plausible. Some stishovite may have inverted to quartz as well as coesite during decompression.

4.1.3. Type III Coesite (Granular grains in maskelynite)

The textures of silica domains (Fig. 2) suggests that the surrounding maskelynite was melted and served as a pressure medium for silica during densification (El Goresy et al., 2004). This is further supported by the pervasive recrystallization of surrounding pyroxene (Fig. 2), as well as the formation of troilite droplets (Fig. 2f). The

morphology of Type III coesite is similar to that of stishovite and seifertite embedded in maskelynite from Shergotty (El Goresy et al., 2004). However, unlike the plgiaocase dissociation to jadeite, stishovite, and CAS (El Goresy et al., 2004), Type III coesite probably formed by the transformation of silica phases. This is evidenced by its co-occurence with silica glass rather than maskelynite (Figs. 2 and 6). Stishovite and/or seifertite may also have played a role in the formation of Type III coesite similar to the processes associated with Type II coesite formation discussed before (Figs. 1c–f and 3). In both Types II and III coesite, the association with deformed quartz suggests that they had similar formation mechanisms.

4.2. P-T constraints

Coesite is the only high pressure polymorph found in NWA 8657. However, its range of morphologies and its co-occurrence with deformed quartz, silica glass, maskelynite, recrystallized pyroxene, and merrillite, could be used to constrain the impact-induced pressures and temperatures.

Peak pressure: As discussed above, the stishovite-like morphology of Type II coesite (Fig. 1 and 3g and h) and association with deformed quartz (Fig. 1e and 3d–f) suggests the transformation of stishovite to coesite. This would mean that the peak shock compression pressure was between 8 GPa (Langenhorst and Deutsch, 2012) and ~30 GPa (Langenhorst and Deutsch, 2012), based on the Al_2O_3 content (Table S1) (Lakshtanov et al., 2007). Furthermore, the defect band (D1 band) position at 490 cm^{-1} and the broad band position at ~457 cm^{-1} of silica diaplectic glasses in NWA 8657 (Fig. S2) suggest that the pressure was higher than 17.8 GPa (Okuno et al., 1999).

Shock temperature: The high volume of melt regions (Fig. S1), pervasive recrystallization of pyroxene in melt zones (Figs. 1, 2, and 5-8), and presence of nanophase coesite (Figs. 5 and 6) suggests that the shock induced melt vein/zones have been melted and quenched at high pressure and the peak shock temperature was higher than the high pressure solidus (Sharp et al., 2015, 2019; Hu and Sharp, 2017). Therefore, the peak shock temperature is estimated to be ~2000 ℃ at least in the melt zones (Sharp et al., 2015, 2019; Gasparik, 1990; Hu and Sharp, 2017; Tomioka and Miyahara, 2017). Silica was probably in solid phase based on the silica phase diagram (Langenhorst and Deutsch, 2012). However, the co-occurrence of silica phase with maskelynite and pyroxene should lower the melting point, resulting in the melting of silica. Moreover, the chemical compositions of large silica grains interstitial to pyroxene and maskelynite (Fig. S2) also contain some Al_2O_3 (~2.5 wt%), TiO_2 (~0.2 wt%), FeO (~0.3 wt%), CaO (~0.5 wt%), Na_2O (~0.7 wt%), and K_2O (~0.2 wt%) (Table S1), which is also consistent with the melting of silica at temperatures below the melting point of pure silica (Langenhorst and Deutsch, 2012).

Under these peak pressure (~18–30 GPa) and temperature (~2000 ℃) conditions, phosphates, merrillite and apatite, the major REE-bearing phases, around the melt zone should transform to tuite (Murayama et al., 1986; Xie et al., 2002). However, tuite was not identified in the margins of the melt zones in NWA 8657 (Figs. 7 and S3). One possible reason is that the merrillite clast was not be heated up to the peak temperature of the melt based on the thermal modeling constraints (Hu and Sharp, 2017). Another potential explanation is that tuite was inverted to merrillite during decompression, which is consistent with the formation of coesite discussed above. Alternatively, phosphates were partially molten and some of them survived in the melt zones (Howarth et al., 2018). The latter hypothesis is supported by the higher REE concentrations of maskelynite in the melt zones compared with maskelynite in the host rock (Howarth et al., 2018).

Shock release is a natural process for any shock-induced meteorites (Gillet and Goresy, 2013). The higher-pressure silica polymorphs (stishovite and/or seifertite) reported in Shergotty, Zagami, NWA 480, and NWA 856 (El Goresy et al., 2000, 2013; Chennaoui Aoudjehane et al., 2005; Sharp et al., 1999) did not transform to coesite during decompression. Faster post-shock cooling rates than those recorded in NWA 8657, thus preserving smaller melt zones/veins could explain this difference. The widespread recrystallization of pyroxene (Figs. 1, 2, and 5–8) and formation of plagioclase (Figs. 7 and 8) in the melt zones from NWA 8657 support slower post-shock cooling rates than in the other martian meteorites (El Goresy et al., 2000, 2013; Sharp et al., 1999; Chennaoui Aoudjehane et al., 2005), favoring the back-transformation of stishovite to coesite, quartz, and silica glass (Langenhorst and Deutsch, 2012). The back transformation of wadsleyite to olivine in Mbale (a highly shocked L chondrite) and back transformation of ringwoodite to olivine in EETA 79001 (an olivine-phyric shergottite), could therefore be considered analogous to what we observe in NWA 8657, involving relatively slow post-shock cooling rates (Walton, 2013; Hu and Sharp, 2017).

5. CONCLUSIONS

We report the discovery of coesite in the basaltic shergottite NWA 8657. Coesite in NWA 8657 has three different morphological types: Type I: a silica-maskelynite assemblage; Type II: needle shaped coesite; and Type III, granular grains of coesite embedded in maskelynite. Although higher pressure polymorphs than coesite have not been identified in NWA 8657, both stishovite-like Type II coesite morphologies and deformed quartz suggest the inversion of stishovite to coesite during decompression. The impact-induced P-T conditions are estimated at ~18–30 GPa and ~2000 ℃ respectively. The relatively slow post-shock cooling rate of the shock-melt regions in NWA 8657 compared with Shergotty, Zagami, NWA 480, and NWA 856 (El Goresy et al., 2000, 2013; Sharp et al., 1999; Chennaoui Aoudjehane et al., 2005) is supported by the large melt regions, widespread recrystallization of pyroxene, and the recrystallization of plagioclase. Back transformation processes of silica phases such as stishovite to coesite, quartz, and silica glass could place unique constraints on impact-induced phase formation in martian samples.

Declaration of Competing Interest

The authors declare that they have no known competing financial interests or personal relationships that could have appeared to influence the work reported in this paper.

ACKNOWLEDGMENTS

We thank executive editor Dr. Jeffrey G. Catalando and A. E. Dr. Chris Herd for handling the manuscript and language polishing, Dr. Jinping Hu and another anonymous referee's constructive suggestions and comments for improving the quality of the manuscript, and Dr. Masaaki Miyahara for helpful discussions. This study was financially supported by the National Natural Science Foundation of China (41573057, 41430105 and 41973062), China Scholarship Council (201804910284), and the key research program of the Institute of Geology & Geophysics, CAS (IGGCAS-201905).

APPENDIX A. SUPPLEMENTARY DATA

Supplementary data to this article can be found online at https://doi.org/10.1016/j.gca.2020.07.021.

REFERENCES

Aoudjehane H. C., Avice G. and Barrat J. A., et al. (2012) Tissint martian meteorite: a fresh look at the interior, surface, and atmosphere of Mars. *Science* **338**, 785–788.

Barrat J.-A., Chaussidon M. and Bohn M., et al. (2005) Lithium behavior during cooling of a dry basalt: An ion-microprobe study of the lunar meteorite Northwest Africa 479 (NWA 479). *Geochim. Cosmochim. Acta* **69**, 5597–5609.

Baziotis I. P., Liu Y. and DeCarli P. S., et al. (2013) The Tissint Martian meteorite as evidence for the largest impact excavation. *Nat. Commun.* **4**, 1404.

Beck P., Gillet P. and Gautron L., et al. (2004) A new natural high-pressure (Na, Ca)-hexaluminosilicate [$(C_axN_{a1\_x})A_{l3+}xS_{i3\_x}x_{O1}1$] in shocked Martian meteorites. *Earth Planet. Sci. Lett.* **219**, 1–2.

Chao E. C. (1967) Shock effects in certain rock-forming minerals. *Science* **156**, 192–202.

Chao E. C., Shoemaker E. M. and Madsen B. M. (1960) First Natural Occurrence of Coesite. *Science* **132**, 220–222.

Chen M., Xiao W. and Xie X. (2010) Coesite and quartz characteristic of crystallization from shock-produced silica melt in the Xiuyan crater. *Earth Planet. Sci. Lett.* **297**, 306–314.

Chennaoui Aoudjehane H., Jambon A. and Reynard B., et al. (2005) Silica as a shock index in shergottites: A cathodoluminescence study. *Meteorit. Planet. Sci.* **40**, 967.

Dachille F., Zeto R. J. and Roy R. (1963) Coesite and Stishovite: Stepwise Reversal Transformations. *Science* **140**, 991–993.

El Goresy A., Dubrovinsky L. and Sharp T. G., et al. (2004) Stishovite and post-stishovite polymorphs of silica in the shergotty meteorite: their nature, petrographic settings versus theoretical predictions and relevance to Earth's mantle. *J. Phys. Chem. Solids* **65**, 1597–1608.

El Goresy A., Dubrovinsky L. and Sharp T. G., et al. (2000) A monoclinic post-stishovite polymorph of silica in the shergotty meteorite. *Science* **288**, 1632–1635.

El Goresy A., Gillet P. and Chen M., et al. (2001) In Situ Finding of Loci of the Fabric Settings of Shock-induced Quartz/Coesite Phase Transition in Crystalline Clasts in Suevite of the Ries Crater. *Germany. Meteorit. Planet. Sci. Suppl.* **36**, A69.

El Goresy A., Gillet P. and Miyahara M., et al. (2013) Shock-induced deformation of Shergottites: Shock-pressures and perturbations of magmatic ages on Mars. *Geochim. Cosmochim. Acta* **101**, 233–262.

Fazio A., Mansfeld U. and Langenhorst F. (2017) Coesite in suevite from the Ries impact structure (Germany): From formation to postshock evolution. *Meteorit. Planet. Sci.* **52**, 1437–1448.

Fritz J. and Greshake A. (2009) High-pressure phases in an ultramafic rock from Mars. *Earth Planet. Sci. Lett.* **288**, 619–623.

Gasparik T. (1990) Phase relations in the transition zone. *J. Geophys. Res. Solid Earth* **95**, 15751–15769.

Gillet P. and Goresy A. E. (2013) Shock Events in the Solar System: The Message from Minerals in Terrestrial Planets and Asteroids. *Annu. Rev. Earth Planet. Sci.* **41**, 257–285.

Goresy A. E. l. D., Sharp T. G. and Prewitt C. T., et al. (2008) Seifertite, a dense orthorhombic polymorph of silica from the Martian meteorites Shergotty and Zagami. *Europ. J. Mineral.* **20**, 523–528.

Greshake A., Fritz J. and Böttger U., et al. (2013) Shear-induced ringwoodite formation in the Martian shergottite Dar al Gani 670. *Earth Planet. Sci. Lett.* **375**, 383–394.

He Q., Xiao L. and Balta J. B., et al. (2015) Petrography and geochemistry of the enriched basaltic shergottite Northwest Africa 2975. *Meteorit. Planet. Sci.* **50**, 2024–2044.

Herd C. D. K., Walton E. L. and Agee C. B., et al. (2017) The Northwest Africa 8159 martian meteorite: Expanding the martian sample suite to the early Amazonian. *Geochim. Cosmochim. Acta* **218**, 1–26.

Howarth G. H., Udry A. and Day J. M. D. (2018) Petrogenesis of basaltic shergottite Northwest Africa 8657: Implications for fO_2 correlations and element redistribution during shock melting in shergottites. *Meteorit. Planet. Sci.* **53**, 249–267.

Hu J. and Sharp T. G. (2017) Back-transformation of high-pressure minerals in shocked chondrites: Low-pressure mineral evidence for strong shock. *Geochim. Cosmochim. Acta* **215**, 277–294.

Hu S., Lin Y. and Zhang T. (2016) Petrography, Mineral Chemistry and Shock Metamorphism of Martian Meteorite NWA 8657, Meteorit. *Planet. Sci.* **Suppl., #6068**.

Imae N. and Ikeda Y. (2010) High-pressure polymorphs of magnesian orthopyroxene from a shock vein in the Yamato-000047 lherzolitic shergottite. *Meteorit. Planet. Sci.* **45**, 43–54.

Irving, A., Kuehner, S., Andreasen, R., et al., 2015. Petrologic and radiogenic isotopic assessment of olivine-phyric, diabasic and microgabbroic shergottites from Northwest Africa, in: Y., M. H. (Ed.), Lunar Planet. Sci. Conf. 46, #2290.

Jambon A., Barrat J. A. and Sautter V., et al. (2002) The basaltic shergottite Northwest Africa 856: Petrology and chemistry. *Meteorit. Planet. Sci.* **37**, 1147–1164.

Jaret S. J., Phillips B. L. and King D. T., et al. (2017) An unusual occurrence of coesite at the Lonar crater. *India. Meteorit. Planet. Sci.* **52**, 147–163.

Kaiser A., Lobert M. and Telle R. (2008) Thermal stability of zircon ($ZrSiO_4$). *J. Europ. Ceram. Soc.* **28**, 2199–2211.

Kayama M., Tomioka N. and Ohtani E., et al. (2018) Discovery of moganite in a lunar meteorite as a trace of H2O ice in the Moon's regolith. *Sci. Adv.* **4**, eaar4378.

Kieffer S. W., Phakey P. P. and Christie J. M. (1976) Shock processes in porous quartzite: Transmission electron microscope observations and theory. *Contrib. Mineral. Petrol.* **59**, 41–93.

Kimura M., Suzuki A. and Kondo T., et al. (2000) Natural Occurrence of High-Pressure Phases, Jadeite, Hollandite,

Wadsleyite, and Majorite-Pyrope Garnet, in an H Chondrite, Yamato 75100. *Meteorit. Planet. Sci.* **35**, A87–A88.
Kimura M., Yamaguchi A. and Miyahara M. (2017) Shock-induced thermal history of an EH3 chondrite, Asuka 10164. *Meteorit. Planet. Sci.* **52**, 24–35.
Kubo T., Kimura M. and Kato T., et al. (2009) Plagioclase breakdown as an indicator for shock conditions of meteorites. *Nat. Geosci.* **3**, 41–45.
Kubo T., Kimura M. and Nishi M., et al. (2008) Formation of Jadeite from Plagioclase: Constraints on the PTt Conditions of Shocked Meteorites. *Meteorit. Planet. Sci.* **43**, 953–964.
Lakshtanov D. L., Sinogeikin S. V. and Litasov K. D., et al. (2007) The post-stishovite phase transition in hydrous alumina-bearing SiO_2 in the lower mantle of the earth. *Proc. Natl. Acad. Sci. USA* **104**, 13588–13590.
Langenhorst F. (1994) Shock experiments on pre-heated alpha- and beta-quartz. 2: X-ray and TEM investigations. *Earth Planet. Sci. Lett.* **128**, 683–698.
Langenhorst F. and Deutsch A. (2012) Shock Metamorphism of Minerals. *Elements* **8**, 31–36.
Langenhorst F. and Poirier J.-P. (2000a) Anatomy of black veins in Zagami: clues to the formation of high-pressure phases. *Earth Planet. Sci. Lett.* **184**, 37–55.
Langenhorst F. and Poirier J.-P. (2000b) 'Eclogitic' minerals in a shocked basaltic meteorite. *Earth Planet. Sci. Lett.* **176**, 259–265.
Leroux H. and Cordier P. (2006) Magmatic cristobalite and quartz in the NWA 856 Martian meteorite. *Meteorit. Planet. Sci.* **41**, 913–923.
Liu L., Zhang J.-F. and Cao Y.-T., et al. (2018) Evidence of former stishovite in UHP eclogite from the South Altyn Tagh, western China. *Earth Planet. Sci. Lett.* **484**, 353–362.
Liu L., Zhang J. and Green H. W., et al. (2007) Evidence of former stishovite in metamorphosed sediments, implying subduction to >350 km. *Earth Planet. Sci. Lett.* **263**, 180–191.
Ma C., Tschauner O. and Beckett J. R., et al. (2016) Ahrensite, γ-Fe_2SiO_4, a new shock-metamorphic mineral from the Tissint meteorite: Implications for the Tissint shock event on Mars. *Geochim. Cosmochim. Acta* **184**, 240–256.
Ma C., Tschauner O. and Beckett J. R., et al. (2015) Tissintite, (Ca, Na, □)$AlSi_2O_6$, a highly-defective, shock-induced, high-pressure clinopyroxene in the Tissint martian meteorite. *Earth Planet. Sci. Lett.* **422**, 194–205.
Ma C., Tschauner O. and Beckett J. R., et al. (2018) Liebermannite, $KAlSi_3O_8$, a new shock-metamorphic, high-pressure mineral from the Zagami Martian meteorite. *Meteorit. Planet. Sci.* **53**, 50–61.
Miyahara M., Kaneko S. and Ohtani E., et al. (2013a) Discovery of seifertite in a shocked lunar meteorite. *Nat. Commun.* **4**, 1737.
Miyahara M., Ohtani E. and Goresy A. E., et al. (2016) Phase transition processes of olivine in the shocked Martian meteorite Tissint: Clues to origin of ringwoodite-, bridgmanite- and magnesiowüstite-bearing assemblages. *Phys. Earth Planet. Inter.* **259**, 18–28.
Miyahara M., Ohtani E. and Ozawa S., et al. (2011) Natural dissociation of olivine to (Mg, Fe)Si_O3 pervoskite and magnesiowüstite in a shocked Martian meteorite. *Proc. Natl. Acad. Sci. USA* **108**, 5999–6003.
Miyahara M., Ohtani E. and Yamaguchi A. (2017) Albite dissociation reaction in the Northwest Africa 8275 shocked LL chondrite and implications for its impact history. *Geochim. Cosmochim. Acta* **217**, 320–333.
Miyahara M., Ohtani E. and Yamaguchi A., et al. (2014) Discovery of coesite and stishovite in eucrite. *Proc. Natl. Acad. Sci. USA* **111**, 10939–10942.
Miyahara M., Ozawa S. and Ohtani E., et al. (2013b) Jadeite formation in shocked ordinary chondrites. *Earth Planet. Sci. Lett.* **373**, 102–108.
Murayama J. K., Nakai S. and Kato M., et al. (1986) A dense polymorph of $Ca_3(PO_4)_2$: a high pressure phase of apatite decomposition and its geochemical significance. *Phys. Earth Planet. Inter.* **44**, 293–303.
Ohtani E., Ozawa S. and Miyahara M. (2017) Jadeite in shocked meteorites and its textural variations. *J. Mineral. Petrol. Sci.* **112**, 1–9.
Ohtani E., Ozawa S. and Miyahara M., et al. (2011) Coesite and stishovite in a shocked lunar meteorite, Asuka-881757, and impact events in lunar surface. *Proc. Natl. Acad. Sci. USA* **108**, 463–466.
Okuno M., Reynard B. and Shimada Y., et al. (1999) A Raman spectroscopic study of shock-wave densification of vitreous silica. *Phys. Chem. Mineral.* **26**, 304–311.
Ono S., Kikegawa T. and Higo Y., et al. (2017) Precise determination of the phase boundary between coesite and stishovite in SiO_2. *Phys. Earth Planet. Inter.* **264**, 1–6.
Ozawa S., Miyahara M. and Ohtani E., et al. (2014) Jadeite in Chelyabinsk meteorite and the nature of an impact event on its parent body. *Sci. rep.* **4**, 5033.
Pang R.-L., Harries D. and Pollok K., et al. (2018) Vestaite, $(Ti^{4+}Fe^{2+})Ti_3^{4+}O_9$, a new mineral in the shocked eucrite Northwest Africa 8003. *Am. Mineral.* **103**, 1502–1511.
Pang R.-L., Zhang A.-C. and Wang S.-Z., et al. (2016) High-pressure minerals in eucrite suggest a small source crater on Vesta. *Sci. Rep.* **6**, 26063.
Sharma S. K., Mammone J. F. and Nicol M. F. (1981) Raman investigation of ring configurations in vitreous silica. *Nature* **292**, 140–141.
Sharp T. G., El Goresy A. and Wopenka B., et al. (1999) A post-stishovite SiO_2 polymorph in the meteorite Shergotty: implications for impact events. *Science* **284**, 1511–1513.
Sharp T. G., Xie Z. D. and de Carli P. S., et al. (2015) A large shock vein in L chondrite Roosevelt County 106: Evidence for a long-duration shock pulse on the L chondrite parent body. *Meteorit. Planet. Sci.* **50**, 1941–1953.
Sharp T. G., Walton E. L. and Hu J. P., et al. (2019) Shock conditions recorded in NWA 8159 martian augite basalt with implications for the impact cratering history on Mars. *Geochim. Cosmochim. Acta* **246**, 197–212.
Spray J. G. and Boonsue S. (2009) Quartz-Coesite-Stishovite Relations and Genesis in Shocked Metaquartzites from the Vredefort Impact Structure. *Meteorit. Planet. Sci. Suppl.* **72**, 5289.
Spray J. G. and Boonsue S. (2018) Quartz-coesite-stishovite relations in shocked metaquartzites from the Vredefort impact structure, South Africa. *Meteorit. Planet. Sci.* **53**, 93–109.
Stoffler D., Keil D., Scott E.R.D. 1991. Shock metamorphism of ordinary chondrites. Geochim. Cosmochim. Acta 55, 3845–3867.
Stähle V., Altherr R. and Koch M., et al. (2008) Shock-induced growth and metastability of stishovite and coesite in lithic clasts from suevite of the Ries impact crater (Germany). *Contrib. Mineral. Petrol.* **155**, 457–472.
Stoffler D. and Langenhorst F. (1994) Shock metamorphism of quartz in nature and experiment: I. Basic observation and theory. *Meteoritics* **29**, 155–181.
Tomioka N. and Miyahara M. (2017) High-pressure minerals in shocked meteorites. *Meteorit. Planet. Sci.* **52**, 2017–2039.
Walton E. L. (2013) Shock metamorphism of Elephant Moraine A79001: Implications for olivine-ringwoodite transformation and the complex thermal history of heavily shocked Martian meteorites. *Geochim. Cosmochim. Acta* **107**, 299–315.

Walton E. L., Sharp T. G. and Hu J., et al. (2014) Heterogeneous mineral assemblages in martian meteorite Tissint as a result of a recent small impact event on Mars. *Geochim. Cosmochim. Acta* **140**, 334–348.

Weisberg M. K. and Kimura M. (2010) Petrology and Raman spectroscopy of high pressure phases in the Gujba CB chondrite and the shock history of the CB parent body. *Meteorit. Planet. Sci.* **45**, 873–884.

Xie X., Minitti M. E. and Chen M., et al. (2002) Natural high-pressure polymorph of merrillite in the shock veins of the Suizhou meteorite. *Geochim. Cosmochim. Acta* **66**, 2439–2444.

Zhang A.-C., Hsu W.-B. and Floss C., et al. (2010) Petrogenesis of lunar meteorite Northwest Africa 2977: Constraints from in situ microprobe results. *Meteorit. Planet. Sci.* **45**, 1929–1947.

Zhang J., Li B. and Utsumi W., et al. (1996) In situ X-ray observations of the coesite-stishovite transition: reversed phase boundary and kinetics. *Phys. Chem. Mineral.* **23**, 1–10.

Zhou Y., Irifune T. and Ohfuji H., et al. (2017) Stability region of $K_{0.2}Na_{0.8}AlSi_3O_8$ hollandite at 22 GPa and 2273 K. *Phys. Chem. Mineral.* **44**, 33–42.

Associate editor: Jeffrey G. Catalano